THE JOURNAL OF PHYSICAL CHEMISTRY C

Article

pubs.acs.org/JPCC

Catalyst-Assisted Pulsed Laser Deposition of One-Dimensional Single-Crystalline Nanostructures of Tin(IV) Oxide: Interplay of VS and VLS Growth Mechanisms at Low Temperature

Samad Bazargan and K. T. Leung*

WATLab and Department of Chemistry, University of Waterloo, Waterloo, Ontario N2L 3G1, Canada

Supporting Information

ABSTRACT: Single-crystalline nanostructures of tin(IV) oxide (TO) are grown with the aid of size-controllable gold nanoisland (GNI) catalysts supported on a Si substrate by using the pulsed laser deposition (PLD) method. The use of gold nanocatalysts with average size between 15 and 50 nm enables the deposition driven by the vapor−liquid−solid growth mechanism to occur at a relatively low temperature (500−700 °C). By controlling the gas atmosphere (O_2 or Ar) and the GNI support (oxidized or H-terminated Si), we are able to produce a variety of TO nanostructures, including one-dimensional nanowires, nanobelts, and nanobricks, as well as cuboid nanoparticles by the PLD method. Scanning electron microscopy and helium ion microscopy show faceted morphology of these nanostructures and reveal the underlying vapor−liquid−solid and vapor−solid growth mechanisms dominant for nanowires and nanobelts and for nanobricks and nanoparticles, respectively. The nanowires exhibit a square cross section (with side length varying from 70 to 90 nm at the base to 10−50 nm near the tip), while the nanobelts have a rectangular cross section (with a width-to-thickness ratio of 2−9) with a remarkably small thickness (5−30 nm). These unique micrometer-long TO nanostructures have not only the largest surface-to-volume ratio but also low-index surfaces, which can be modified with different deposition parameters. X-ray diffraction study further shows the expected tetragonal crystalline phase of these TO nanostructures but each with its own preferred growth orientation(s): (101) for the nanoparticles and nanobricks, (200) for the nanowires, and (200) and (101) for nanobelts. For nanowires and nanobelts, transmission electron microscopy confirms the single-crystalline nature of these one-dimensional nanostructures, with their different growth orientations that lead to the preferred growth directions as collaborated by the corresponding X-ray diffraction data. These results demonstrate the versatility of the catalyst-assisted PLD method in fabricating novel one-dimensional TO nanostructures, with good control on not only their shapes and cross-sectional dimensions and their aerial densities but also their growth orientations and side surface planes. The catalyst-assisted PLD method can easily accommodate doping and other fabrication steps to incorporate desirable semiconducting, gas-sensing, optoelectronic, and magnetic properties in these one-dimensional TO nanostructures for emerging applications.

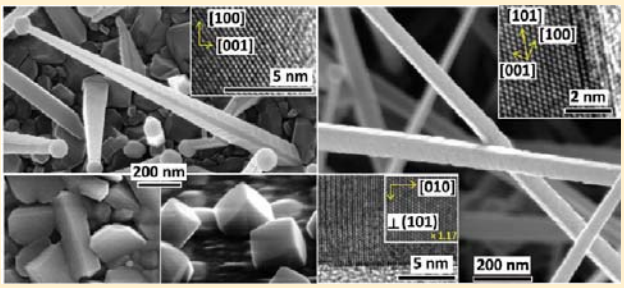

1. INTRODUCTION

One-dimensional (1D) nanostructures have received considerable attention due to their unique properties originating from their nanoscale dimensions, large length-to-width aspect ratio, highly crystalline faceted structures with low index surfaces, and high surface-to-volume ratios. In addition to the interesting mechanical and chemical properties arising from these nanostructures and their surfaces, novel electrical and optical properties can also be observed due to their single-crystalline structure with sizes comparable to the characteristic optical and electrical length scales, i.e., the wavelength of visible light and Debye length, respectively. Synthesis of 1D semiconducting oxides, both pristine and doped forms, is of special interest because of their rich potential applications resulting from their semiconducting,[1] gas-sensing,[2] optoelectronic,[3] magnetic,[4,5] and optical properties.[6,7] A variety of fabrication techniques have been employed to synthesize 1D nanostructures, and they include thermal evaporation[8] or laser-assisted ablation,[9] template-based methods,[10−12] and solution-phase syntheses.[13] In the thermal evaporation and laser ablation methods,[8,9] a precursor material is evaporated either thermally[14] or by using a laser beam[3,15] in a tube furnace, and the precursor vapor is then thermalized and transported downstream by a carrier gas to undergo further reactions or deposition onto a substrate at an appropriate temperature. These methods have been widely used, often with the addition of an appropriate catalyst, for synthesizing a variety of 1D nanostructures, including Si and Ge,[9] a wide range of III−V and II−VI semiconductors such as GaAs and CdS,[16] and semiconducting oxides.[14] Among the wide bandgap semiconducting oxides, tin(IV) oxide (TO) is particularly interesting because of its high sensitivity toward adsorbed gases,[17,18] high chemical and thermal stability,

Received: December 1, 2011
Revised: February 8, 2012
Published: February 8, 2012

   dx.doi.org/10.1021/jp211553j | J. Phys. Chem. C 2012, 116, 5427−5434

mechanical durability,[19] optoelectronic properties,[3] and its special magnetic properties upon appropriate doping.[4,5] Different 1D TO nanostructures, including nanowires and nanobelts, have been produced by a number of methods, including thermal evaporation of Sn[20] and SnO powders,[8] laser ablation of Sn[3] and SnO_2 targets,[15] and plasma-enhanced CVD,[21] sol−gel method,[22] solution-phase synthesis,[23] and spray pyrolysis method.[24] However, the control on the nucleation sites, size distribution, and crystalline growth orientation of the 1D nanostructures remains difficult to achieve in the synthesis of these nanostructures. Property modification of 1D nanostructures of TO or other oxides through appropriate doping is also another factor, which is crucial for obtaining the required functionalities of oxide materials, and has not been extensively addressed in the literature.

Unlike the thermal evaporation and the aforementioned chemical deposition methods, pulsed laser deposition (PLD) involves direct laser ablation of the target material into the gas phase, which is then exposed to the substrate held at a specified temperature. This leads to the deposition of material through a growth mechanism far from thermal equilibrium. Because of the high deposition rate as a result of the energetic plasma and the high ablation rate of the target materials, especially suitable for those with a high melting point, the PLD method has been extensively used for depositing thin-film oxide materials.[25,26] In particular, high quality epitaxial growth on a substrate with a good lattice match to the oxide material of interest can be achieved by using the PLD method in high vacuum.[27,28] Furthermore, because laser ablation maintains the stoichiometry of the target material, PLD is also especially suitable for obtaining doped materials using predoped targets,[4,5,29,30] which is particularly important for modifying the properties of oxide materials. In comparison to the laser-assisted catalytic growth of Si and III−V semiconductors,[9,16] and other laser-ablation studies performed in tube furnace (with limited vacuum no better than 10^{-3} mbar),[3,15] PLD is a high-vacuum deposition technique that allows a considerably better control on the composition of the process gas, which, as discussed below, plays an important role in the deposition. Furthermore, the control of the substrate-to-target distance in the PLD technique can be used to expose the substrate to the nonthermalized region of the plasma, resulting in improved diffusion of the deposited atoms,[31] while deposition with multiple targets without exposure to air facilitates homo- and heteroepitaxial growth of nanostructures. These additional controls in the PLD method could lead to the growth of 1D nanostructures with new structural properties and desirable composition, morphology, and growth orientation. To date, these fundamental advantages of the PLD technique have been largely overlooked in the synthesis of 1D nanostructures. Tien et al.[32] have reported PLD synthesis of TO films with small columnar grains that leads to formation of nanorods, without any regular cross-sectional morphology, densely packed into a film. However, no discrete TO nanobelts or nanowires synthesized by PLD have hitherto been reported.

Like the study by Tien et al.,[32] we verify that the PLD technique can be used to produce nanostructured TO films with columnar granular morphology on Si substrates. However, by first depositing Au as a catalytic seed layer on the substrate, we succeed in obtaining 1D TO nanostructures by using the PLD method. In order to activate the Au catalyst (mp 1064 °C[33]) and initiate a vapor−liquid−solid (VLS) growth, deposition temperature above 1000 °C is usually required.[8] Such a high deposition temperature, which has been traditionally used in the aforementioned thermal evaporation and laser-ablation methods, is difficult to achieve in PLD systems. We demonstrate that activation of the catalyst can occur at a lower temperature for nanosized Au islands, i.e., hemispherical nanoparticles, allowing the VLS growth to proceed at a considerably lower temperature. This catalyst-assisted PLD technique opens up a general approach to fabricating 1D nanostructures of oxides, with all the aforementioned advantages of the PLD technique not found in the other methods. Moreover, by modifying the deposition conditions (including the process gas and its pressure, substrate temperature, substrate-to-target separation, and laser fluence and repetition rate) to favor nanocrystalline growth over thin-film deposition, it is possible to produce a variety of nanostructures, including nanowires, nanobelts, nanoparticles, and nanobricks. The nanometer size of the catalysts is also found to be naturally effective in reducing the cross-sectional dimension of these 1D TO nanostructures well below 50 × 90 nm^2, making them the smallest (and hence with the largest surface area-to-volume ratio) ever reported. These results pave the way to extending the application of catalyst-assisted PLD to controlling the growth orientation epitaxially on appropriate substrates and to doping of semiconducting oxides.

2. EXPERIMENTAL DETAILS

The NanoPLD system (PVD Products) used for the present work has a base pressure of 8 × 10^{-8} Torr and has been described in detail elsewhere.[34] A KrF excimer laser (248 nm wavelength) operated with a laser fluence of 100−600 mJ/pulse at a repetition rate of 1−10 Hz is used to ablate a tin(IV) oxide target, which is prepared by cold-pressing SnO_2 powders (Aldrich, 99.90% purity) with a pressure of 20 MPa followed by sintering at 900 °C for 24 h. Si(100) chips chemically oxidized by using a RCA cleaning method (ox-Si)[35] or H-terminated by HF etching after cleaning (H-Si) have been used as substrates for deposition, with the substrate temperature varied from room temperature to 900 °C by radiative heating with infrared heat lamps. To produce the catalytic seed layer, we first deposit a thin layer of gold (5−15 nm thick) on the substrate by magnetron sputtering, and gold nanoislands (GNIs) with an average size of 10−50 nm and a Gaussian size distribution are formed by postannealing in O_2 for ox-Si substrates or in Ar for H-Si substrates, at 400−700 °C, depending on the required average size, for 1 h. To differentiate the importance of the substrate interface in the preparation of the GNIs and their effects on the subsequent PLD growth of TO nanostructures, we designate them as GNI/ox-Si and GNI/H-Si templates. The details of obtaining different average sizes of the GNIs (from 10 to 50 nm) have been discussed by Sohn et al.[36]

Using the GNI catalysts so prepared, TO nanostructures are deposited on the Si substrate, kept at 50 mm from the target, where the substrate is in close proximity of the visible plasma range. Deposition is performed by operating the laser at a fluence of 350 mJ/pulse with a repetition rate of 5 Hz for a period of either 60 or 90 min, while the substrate temperature is maintained at 500, 600, or 700 °C in a 400 mTorr atmosphere of Ar or O_2 (upon evacuating the chamber to the base pressure). The surface morphologies of the as-deposited samples are examined by using a Zeiss ORION Plus helium ion microscope (HIM) and a LEO FESEM 1530 scanning electron microscope (SEM), and their crystal structures are determined

dx.doi.org/10.1021/jp211553j | J. Phys. Chem. C 2012, 116, 5427−5434

by glancing-incidence X-ray diffraction (GIXRD) at an incidence angle of 0.3° in a PANalytical MRD X'pert Pro diffractometer with a Cu Kα source. Crystalline structures of individual nanostructures are studied by using a JEOL 2010F transmission electron microscope (TEM) operated at 200 kV.

3. RESULTS AND DISCUSSION

Figure 1a shows the HIM images of a typical TO film PLD-grown at 500 °C for 60 min in 400 mTorr of Ar on a H-Si substrate without GNIs. A closely packed granular morphology with a grain size of 50−70 nm is observed, while the faceted nanostructures become evident with HIM imaging. Moreover, the corresponding cross-sectional HIM image (Figure 1a, inset) shows the columnar structure of the grains with faceted irregular shapes that extend over the thickness of the film. Similar morphology with a notably larger grain size (50−100 nm) is also found for the film grown in 400 mTorr of O_2 on an ox-Si substrate without GNIs (Figure 1b and inset). Furthermore, the granular film morphology for deposition on an ox-Si substrate in 400 mTorr of Ar (not shown) is similar to that obtained on H-Si in Ar atmosphere (Figure 1a). These results illustrate that the process gas has a greater effect on the growth rate of TO grains than the surface chemistry of the Si substrate, resulting in a slower growth rate in Ar gas for both H-Si and ox-Si substrates than that in O_2.

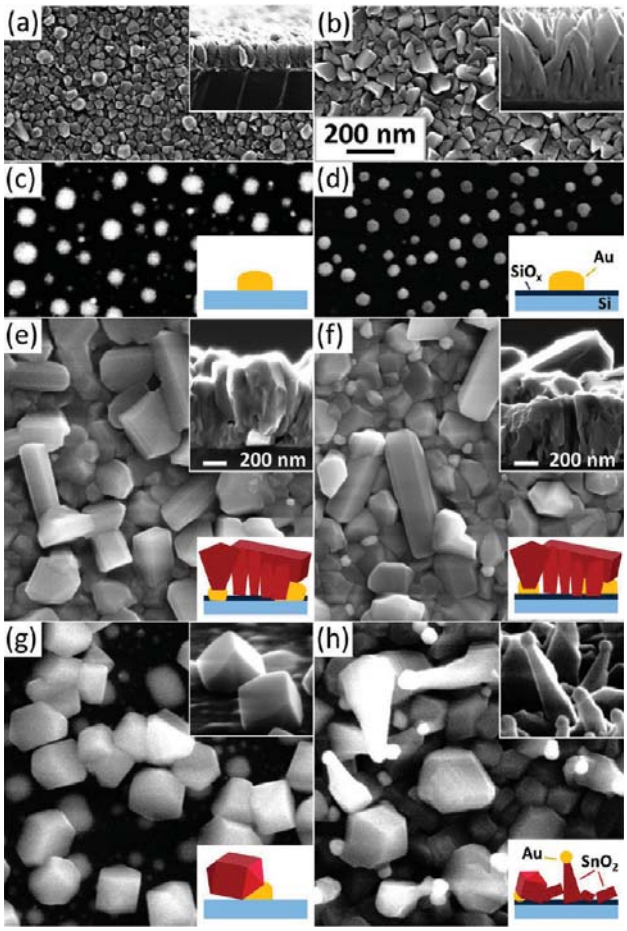

Figure 1. HIM images of typical TO films deposited on (a) a H-Si substrate in 400 mTorr of Ar and (b) an ox-Si substrate in 400 mTorr of O_2, all at 500 °C with corresponding cross-sectional HIM images shown as top insets, and SEM images of gold nanoislands (GNIs) on (c) a H-Si substrate (GNI/H-Si) and (d) an ox-Si substrate (GNI/ox-Si), and of the TO nanostructures grown on (e) a GNI/H-Si and (f) a GNI/ox-Si templates in 400 mTorr of O_2, with the corresponding cross-sectional HIM images shown as top insets, and on (g) a GNI/H-Si and (h) a GNI/ox-Si templates in 400 mTorr of Ar, all at 700 °C with the corresponding SEM images collected at 70° tilt shown as top insets. Lower insets schematically show the GNI/H-Si and GNI/ox-Si templates and the PLD-grown TO nanostructures on the H-Si and ox-Si substrates with GNIs. Except for top insets of (e) and (f), the scales for all images (including the insets) are the same as (b).

Figures 1c and 1d show the SEM images of typical GNI templates supported on a H-Si and an ox-Si substrates, respectively, which are used to guide the growth evolution and to control the morphology of the TO nanostructures during the PLD growth. Evidently, GNI/H-Si appears to exhibit a broader Au nanoisland size distribution than GNI/ox-Si. The formation of Au silicide is expected to proceed more readily on a H-Si than an ox-Si substrate,[36] which causes the GNIs to adhere more strongly to and therefore less likely to be lifted off H-Si than ox-Si substrate. In order to investigate the effects of different processing gases, we deposit TO nanostructures on the two supported GNI templates in 400 mTorr of O_2 and of Ar. In particular, faceted nanostructures containing "nanobricks" with distorted tetragonal shapes and "nanogravels" with more tile-like shape are observed for the highly crystalline TO films PLD-grown in O_2 on both GNI/H-Si (Figure 1e) and GNI/ox-Si templates (Figure 1f). The observed nanobricks (approximately 100 × 100 × 500 nm^3 in size) and nanogravels (200 × 200 nm^2 in area) are found to be considerably larger than the granular structures in the TO films PLD-grown on the substrates without GNIs (Figure 1a,b), suggesting that the GNIs function as an effective catalyst. In a separate slice-and-view study conducted with a focused ion beam SEM, we observe that the large faceted nanostructures mainly grow on top of the GNIs, which remain in contact with the substrate (Supporting Information, Figure S1), in good agreement with the cross-sectional HIM images of these samples (top insets of Figure 1e,f). Although the growth begins with nucleation on the GNI sites, further evolution toward the faceted nanostructures appears to follow a vapor−solid growth mechanism, leading to almost total covering of the GNIs by the TO nanostructures on top. As reported for vapor−solid growth mechanism in earlier studies,[14] the presence of a catalyst can change the surface energies of crystalline planes of the nanostructures. This is in good accord with the present observation that the supported GNI templates act as a catalyst and promote the growth of single-crystalline, faceted TO nanobricks and nanogravels in the PLD process.

On the other hand, the nanostructured TO films PLD-grown in Ar on the GNI/H-Si (Figure 1g) and GNI/ox-Si templates (Figure 1h) are found to be notably different from each other and from those PLD-grown in O_2 (Figure 1e,f). In particular, faceted cuboid nanostructures terminated with square pyramids are preferentially grown on the GNI sites and not on the bare areas of the H−Si substrate, leading to the formation of discrete nanoparticles instead of a continuous film (Figure 1g). Growth of these individual cuboid nanoparticles therefore suggests that GNIs act as nucleation sites, similar to the case of nanobricks. The growth continues with the preferential absorption of vapor from the ablated target in GNIs (VLS growth mechanism) and/or their preferential adsorption on TO surfaces (VS growth mechanism), while no TO growth occurs on the bare H-Si

dx.doi.org/10.1021/jp211553j | J. Phys. Chem. C 2012, 116, 5427−5434

areas. With the exception of those nanoparticles that grow into one another, the discrete nanoparticles appear to be quite uniform in size (with ~200 nm edge length). Remarkably, the film PLD-grown on GNI/ox-Si in Ar (Figure 1h) exhibits prominent nanospike structures with the GNIs on top. The nanospikes are found to be randomly oriented and have multiple facets along their 200−500 nm length. The presence of GNIs on top of the nanospikes (Figure 1h, top inset) is indicative of a predominantly VLS growth mechanism, commonly found for 1D nanostructure growth in previously reported laser-assisted catalytic growth processes.[9,16] Furthermore, a limited number of faceted cuboid nanostructures similar to those obtained on GNI/H-Si in Ar (Figure 1g) are also observed, along with smaller grains among the nanospikes and cuboid nanoparticles. The coexistence of the vapor−solid growth mode operative for these latter nanostructures with the VLS growth mechanism found for the nanospikes highlights the complexity of the growth process for nanostructures obtained in Ar atmosphere.

Figures 2a and 2b show the SEM images of 1D TO nanostructures PLD-grown on a GNI/ox-Si template, with an

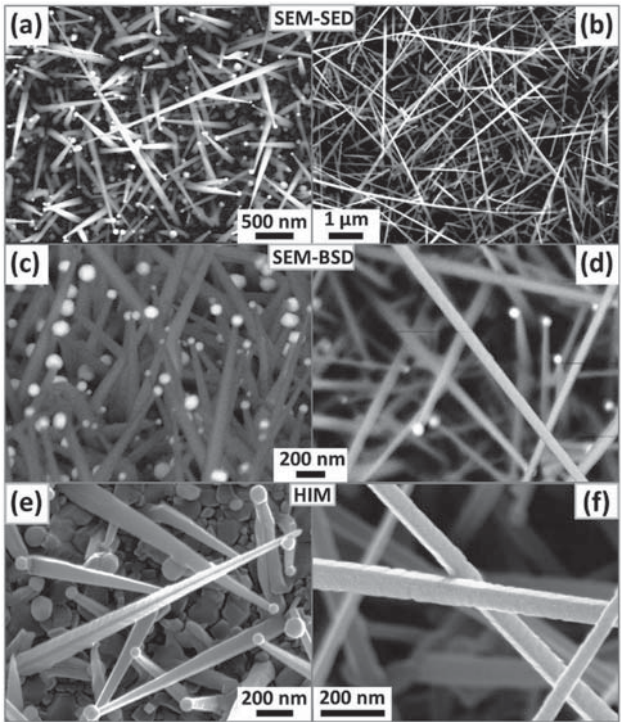

Figure 2. SEM images of (a) nanowires and (b) nanobelts, PLD-grown on an GNI/ox-Si template in 400 mTorr of Ar for 90 min at 600 and 500 °C, respectively, collected by using the in-lens secondary electron detector (SED) and by using the backscattered electron detector (BSD) with a higher elemental contrast at a higher magnification for (c) nanowires with a 70° tilt and (d) nanobelts. HIM images collected at a higher magnification for (e) nanowires and (f) nanobelts.

average GNI size of 50 nm, in 400 mTorr of Ar for 90 min at lower substrate temperatures of 600 and 500 °C, respectively. Unlike the case of nanoparticles (Figure 1g) and nanobricks (Figure 1e,f) but similar to that found for the nanospikes (Figure 1h) grown at 700 °C, the GNIs are found to detach from the substrate, and they stay on top of the growing nanostructures, as illustrated in the SEM backscattered electron images at a higher magnification (Figure 2c,d), clearly revealing the VLS growth mechanism for these nanostructures. The nanowires PLD-grown in Ar at 600 °C have a nearly square-shaped cross section (Figure 2e), the size of which reduces from 70 to 90 nm side length at the base to 15−50 nm side length at the tip along their typical 1−5 μm length (Figure 2c). There is no evidence of Au consumption due to incorporation into the TO nanostructure in the energy-dispersive X-ray mapping studies performed with TEM measurement (results not shown). The observed tapering of the nanowires can therefore be attributed to the following two effects. First, the observed shape evolution of the dome-shaped Au nanoislands to more spherical nanodroplets with increasing deposition time could be attributed to the superficial heating effect of plasma. This shape evolution reduces the active contact area for the VLS growth, which in turn causes reduction in the nanowire cross section. This results in the observed smaller nanowire cross section at the tip than the diameter of the Au nanodroplet. Second, the larger cross section found at the base of nanowires in comparison to the size of the GNI at the tip could be due to vapor−solid growth occurring concurrently, as observed in the formation of nanobricks and nanoparticles. In particular, as the nanowires grow longer, more vapor-to-solid deposition occurs around the side surfaces of the nanowires, causing tapering from the base area, with a longer exposure, to the tip area, with a shorter exposure. On the other hand, the nanobelts PLD-grown in Ar at 500 °C, shown in the HIM image (Figure 2f), have a distinctly rectangular cross section, with a typical thickness of 5−30 nm and width of 30−70 nm, giving an aspect ratio of 2−9. Unlike the 1−5 μm long nanowires, these nanobelts appear to grow to tens of micrometers in length in 90 min. Because of the faster growth rate of nanobelts, the cross sections of the nanobelts exhibit only a minor reduction along the length, which is most notable within 1 μm from the tip and could be attributed to the termination and cooling stage of the PLD process.

The presence of an oxide layer on the Si substrate prevents strong binding of GNIs to the Si substrate and is therefore crucial for the detachment of GNIs from the substrate and initiation of the VLS growth. Without such an oxide layer, deposition of Au has been found to produce an interfacial gold silicide layer on a (pristine) Si substrate.[36] Moreover, deposition in O_2 leads to the coverage of GNIs by a TO layer, while deposition in Ar gives rise to formation of 1D nanospikes, nanowires, and nanobelts predominantly through the VLS mechanism. The lack of oxygen and the plausible high solubility of oxygen-deficient TO clusters from the plasma in gold can account for the effect of the Ar atmosphere on the VLS growth of 1D TO nanostructures. Since the nanobelts and nanowires both have a general four-sided cross section (i.e., rectangular and square, respectively) and grow symmetrically perpendicular to this cross section, the deposition temperature (500 °C for nanobelts, 600 °C for nanowires) is therefore the key parameter that controls the growth rate leading to the observed differences in their shapes and lengths. It has been proposed that the growth rate in the VLS mechanism is governed by the pseudobinary phase diagram of TO and the Au catalyst, in which the temperature directly affects the eutectic phase transition of the supersaturated liquid leading to precipitation and growth of the nanostructure in the VLS growth mechanism.[16] The lower growth temperature also appears to affect the growth rates along different planes, the

dx.doi.org/10.1021/jp211553j | J. Phys. Chem. C 2012, 116, 5427−5434

difference of which creates the rectangular cross-sectional shape for the nanobelts (This effect will be discussed in more detail in the TEM section.)

In addition to the effect of the deposition temperature, we also investigate the effects of the size of GNI catalysts on the PLD growth of these nanostructures. The average size of the GNIs formed on a Si substrate can be easily controlled by adjusting the thickness of the deposited Au film and the postannealing temperature, as described in detail by Sohn et al.[36] Figures 3a and 3b show the HIM images of two GNI/ox-Si

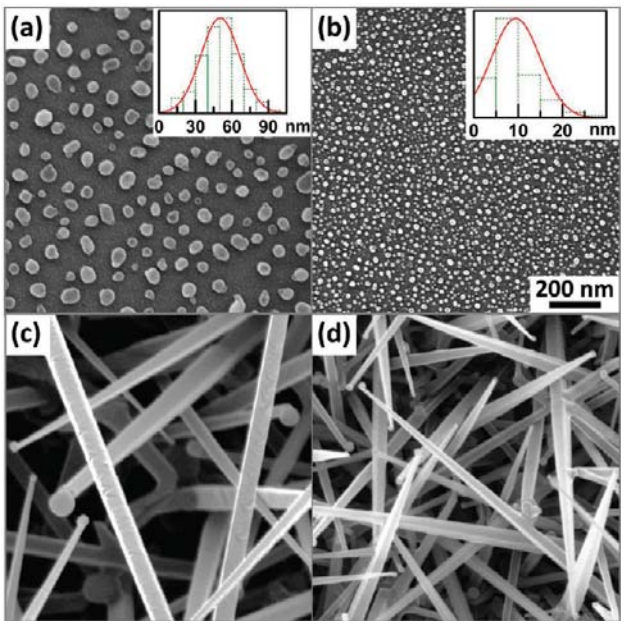

Figure 3. HIM images of the gold nanoislands (GNIs) prepared on ox-Si substrates with average diameters of (a) 50 nm and (b) 10 nm, and Gaussian size distributions (insets), and the HIM images of the nanobelts (c) and (d) PLD-grown in 400 mTorr of Ar at 500 °C for 90 min on the GNI/ox-Si templates shown in (a) and (b), respectively. All the images share the same scale bar shown in (b).

templates with near-Gaussian GNI size distributions and average GNI sizes of 50 and 10 nm, respectively, and the corresponding TO nanostructures PLD-grown in 400 mTorr of Ar for 90 min at 500 °C on these GNI templates. In spite of the smaller dimensions of these nanostructures obtained on the 10 nm GNI template (Figure 3d) compared to those grown on the 50 nm GNI template (Figure 3c), high-resolution HIM reveals their distinct nanobelt morphology, with the characteristic rectangular cross sections. These nanobelts have a generally smaller cross section but still exhibit a width-to-thickness ratio similar to the nanobelts PLD-grown using the 50 nm GNI template. The nanobelts deposited on the 10 nm GNIs (Figure 3d) are found to be shorter (1−2 μm in length) than those on the 50 nm GNIs (10−30 μm in length), which leads to their more vertical orientations with respect to the substrate. The 10 nm GNI template (Figure 3b) also has a higher GNI aerial density than the 50 nm GNI template (Figure 3a), which leads to a correspondingly higher density of and therefore smaller spacings among the nanobelts. The increase in the aerial density with the correspondingly smaller size of the GNIs reduces the overall amount of the TO vapor absorbed by each GNI, which consequently leads to a shorter nanobelt length. The present result therefore shows that the size and distribution of the GNI catalysts can be used to effectively control the cross-sectional dimension (while only the growth temperature governs the width-to-thickness ratio), longitudinal growth rate, and the aerial density of the deposited 1D TO nanostructures prepared using this catalyst-assisted PLD method. This type of control is possible because of the VLS growth mechanism occurring at the catalyst location that is responsible for the growth of these 1D nanostructures.

Figure 4 shows the corresponding GIXRD patterns of the aforementioned TO nanostructured films with predominant

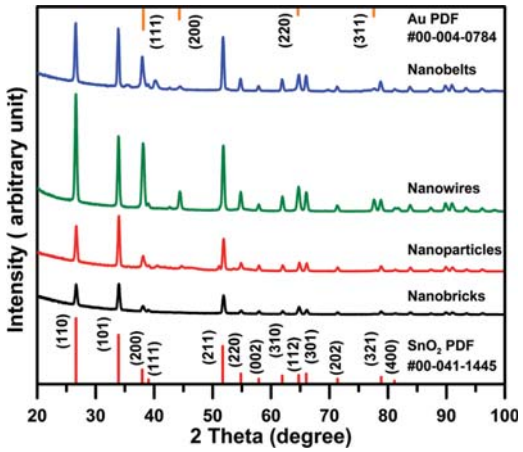

Figure 4. Glancing-incidence XRD patterns of different TO nanostructures obtained at an incidence angle of 0.3°. The PDF2 reference patterns of the tetragonal phase of SnO_2 powder (#00-041-1445) and fcc phase of Au (#00-004-0784) are shown as bottom and top bar graphs, respectively.

nanobricks and nanogravels (Figure 1f), nanoparticles (Figure 1g), nanowires (Figure 2a), and nanobelts (Figure 2b). Evidently, in addition to the observed crystalline peaks of the fcc phase of Au (PDF2 #00-004-0784), a single tetragonal phase of SnO_2 (PDF2 #00-041-1445) is observed for all the nanostructures. These results show that the different growth conditions, particularly deposition in an Ar atmosphere, have not affected the crystalline structure of these nanostructures, which verifies that the stoichiometry of the SnO_2 target is preserved in the PLD growth of all the deposited TO nanostructures. In spite of the nanometer size of these nanostructures, the observed peak widths are within the instrumental resolution, indicative of the high level of crystallinity with minimal strains in these nanostructures. Of particular interest are the remarkably different relative peak intensities, most notably for the prominent diffraction peaks, found for the different TO nanostructures shown in Figure 4. With respect to the reference pattern for SnO_2 powder (PDF2 #00-041-1445), the differences in the relative intensities for different PLD-grown nanostructures show that they all have a preferred growth orientation: (101) for nanoparticles and nanobricks, (200) for nanowires, and (200) and (101) for nanobelts (Figure 4). We summarize the intensities of the (101) and (200) peaks relative to the (110) peak (the most intense peak in the reference pattern) for different nanostructures in Table 1. Evidently, the intensity ratios for (101) to (200) for the nanoparticles (7.9) and nanobricks (5.0) and for the nanowires (2.3) and nanobelts (2.2) are respectively larger and smaller than that of the reference (3.6). Moreover, nanobelts show a high intensity ratio (0.98) for the (101) peak

dx.doi.org/10.1021/jp211553j | J. Phys. Chem. C 2012, 116, 5427−5434

Table 1. Comparison of the Intensities of Different Peaks Relative to (110) for the GIXRD Patterns of Different Predominant TO Nanostructures to Those of the Reference Pattern for SnO_2 Powder (PDF2 #00-041-1445)

	peak intensity relative to (110)	
SnO_2 nanostructures	(101)	(200)[a]
ref pattern PDF2 #00-041-1445	0.75	0.21
nanoparticles	1.43	0.18
nanobricks	1.31	0.26
nanowires	0.65	0.28
nanobelts	0.98	0.44

[a]Intensity of the SnO_2 (200) peak at 38.1° is calculated by removing the contribution of the nearby Au (111) peak, estimated by using the observed Au (220) peak intensity appropriately scaled with the corresponding intensity ratio (0.52) obtained from the Au reference pattern, PDF2 #00-004-0784.

relative to (110) peak, while the nanowires exhibit a smaller ratio (0.65) than that of the reference (0.75). These results suggest that the differences in the morphology of the nanostructures obtained by modifying the deposition parameters are caused by changes in the crystalline growth orientations of these nanostructures.

Typical low-resolution TEM images, along with their selected area electron diffraction (SAED) patterns, obtained for the TO nanowires and nanobelts are shown in Figure 5. For a straight section of the nanowire without any sign of mechanical bend or twist (Figure 5a), the corresponding SAED pattern reveals a growth direction perpendicular to the (200) plane, i.e., along the length of the nanowire in the [100] direction. The crystalline orientations in this nanowire inferred from the SAED pattern are also shown schematically using a ball-and-stick model of the SnO_2 unit cell in Figure 5a. Moreover, it is revealed that the nanowire has the (010) planes [equivalent to the (100) plane due to symmetry of the tetragonal structure] as its side surfaces perpendicular to the zone axis and the (001) planes as the other side surfaces parallel to the zone axis. The measured lattice spacings (a, b = 4.74 Å and c = 3.19 Å) and the observed diffraction pattern are in excellent agreement with the tetragonal crystal structure of SnO_2. The high-resolution TEM image taken at the edge of the nanowire (Figure 5a, right) confirms the observed growth orientation of [100] (marked by a long arrow in Figure 5a) with the measured lattice spacing of 4.74 Å. Other high-resolution images taken across the nanowires (not shown) show no discernible lattice defects with essentially identical lattice constants. Furthermore, high-resolution TEM images collected over a large scan area (not shown) do not show any fault line in the crystal structure of the nanowire.

Figures 5b and 5c show the TEM images obtained for two nanobelts, which are selected to illustrate the different possible growth orientations within a single PLD-grown nanobelt sample. The observed differences in contrast for different sections of the nanobelts (Figure 5b,c) are the result of mechanical twists and bends along the length (10−30 μm) of the nanobelts (Figure 2b). The corresponding SAED patterns reveal different growth orientations along their length in the [010] (Figure 5b) and [101] directions (Figure 5c) in these

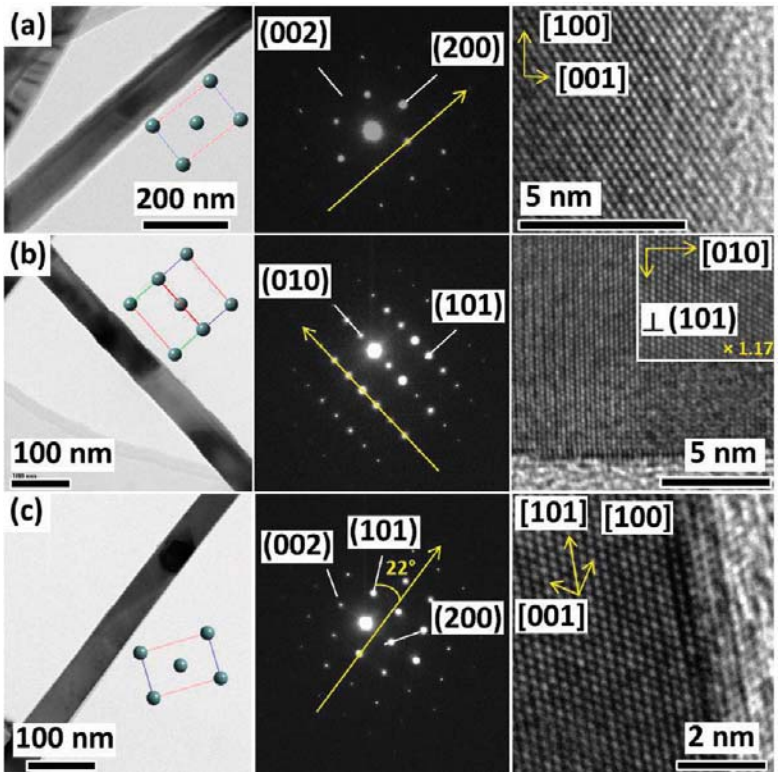

Figure 5. Low-resolution TEM images (left) with their corresponding SAED patterns (center) and high-resolution TEM images (right) with spacings corresponding to different crystalline planes for (a) nanowire and (b, c) nanobelts with different growth orientations. The ball-and-stick models of the SnO_2 unit cell show the crystalline orientations of the nanostructures, and the extracted crystal directions are indexed in the SAED patterns, with the growth directions marked by long arrows.

dx.doi.org/10.1021/jp211553j | J. Phys. Chem. C 2012, 116, 5427−5434

nanobelts. The SAED patterns further show that the nanobelts have (101) planes as their narrow side surfaces parallel to the zone axes (Figure 5b,c), while they show different planes perpendicular to the [10−1] (Figure 5b) and [010] (Figure 5c) zone axes on their wide side surfaces. The plane perpendicular to the [010] axis is the (010) or equivalently (100) plane, while the closest plane perpendicular to the [10−1] axis is the (201) plane with a 87.3° angle. The corresponding high-resolution TEM images show the single-crystalline nature of the nanobelt structure, and the measured lattice spacings of 2.38 and 2.64 Å correspond to the [010] (Figure 5b, right) and [101] directions (Figure 5c, right), respectively, which confirm the growth directions identified in their respective SAED patterns.

The different growth orientations found in these nanobelts leading to growth in the (101), (100), and (201) planes are in good agreement with our XRD results (Figure 4), which indicate a preferred growth orientation in comparison to the reference polycrystalline SnO_2 pattern for both the (200) and (101) planes. The observed preferred growth of the nanowires for the (200) peak in the GIXRD results (Figure 4) can also be explained by the observed side planes of (100) and (001), where the former will produce the observed high intensity of the (200) peak. The presence of different growth planes for nanowires and nanobelts can also account for the observed differences in the cross-sectional morphologies, where different growth rates are expected for different planes. The formation of the (001) side planes, which possess the highest surface energy among the low-index planes of TO,[37] for nanowires suggests that the higher deposition temperature of 600 °C, in comparison to 500 °C for nanobelts, provides sufficient energy for the growth of this plane. The higher growth rates expected for the high-energy surfaces can therefore explain the observed square cross-section of the nanowires, in contrast to the rectangular cross-section of the nanobelts, where the other side plane has a lower growth rate than the (101) side plane. These results indicate that the catalyst-assisted PLD method provides adequate energy for growth in different low-index directions and that the deposition parameters, particularly the growth temperature, can be used to control these orientations leading to different morphologies.

4. CONCLUSIONS

The present study demonstrates that a variety of single-crystalline nanostructures of TO can be synthesized by modifying the deposition parameters using a catalyst-assisted PLD technique, paving the way for further growth studies of these intricate oxide nanostructures by this method. Deposition parameters, including the substrate temperature and the composition of the process gas (O_2 or Ar), and the type of support for the GNI template (ox-Si or H-Si) are all found to have strong effects on the morphology of the resulting nanostructures. At 700 °C, faceted nanobricks are obtained on a GNI/ox-Si template in O_2, while faceted nanoparticles are grown on a GNI/H-Si template in Ar, mainly through a catalytic vapor−solid growth mechanism. On the other hand, nanospikes are obtained on a GNI/ox-Si template in Ar at 700 °C, through a catalytic vapor−liquid−solid mechanism. Furthermore, reducing the deposition temperature leads to the growth of micrometer-long nanowires at 600 °C and nanobelts at 500 °C, all with remarkably small cross-sectional dimensions. We demonstrate for the first time that by creating a supported GNI template, it is possible to promote VLS growth (in preferred orientations) at a relatively low temperature by using PLD and to produce a variety of 1D TO nanostructures. Furthermore, not only the length of the nanobelts and nanowires can be controlled by the deposition time, their width and density on the surface can also be modified by varying the size and density of the GNIs on the substrate. In addition, X-ray diffraction data confirms the presence of the tetragonal SnO_2 crystalline phase and a preferred growth orientation of (200) for nanowires, (200) and (101) for nanobelts, and (101) for nanobricks and nanoparticles. TEM results further show the single-crystalline structures of the nanobelt and nanowire and reveal the different growth orientations of these 1D nanostructures in excellent accord with our XRD data. The present work therefore demonstrates the potential of the catalyst-assisted PLD technique as a general approach to the synthesis of single-crystalline 1D nanostructures of other oxide materials, with controllable morphologies and dimensions, at a relatively low temperature. With their high surface area and in a selected number of low-index surface planes, these 1D TO nanostructures offer a unique opportunity to exploit the selectivity and reactivity of their surface chemistry in a variety of applications, including chemical sensing. Moreover, this method can easily accommodate the introduction of dopants for developing new or optimizing existing properties of these TO nanostructures for opto/electronics applications.

■ ASSOCIATED CONTENT

Supporting Information

Figure S1. This material is available free of charge via the Internet at http://pubs.acs.org.

■ AUTHOR INFORMATION

Corresponding Author

*E-mail: tong@uwaterloo.ca.

Notes

The authors declare no competing financial interest.

■ ACKNOWLEDGMENTS

The present work was supported by the Natural Sciences and Engineering Research Council of Canada.

■ REFERENCES

(1) Wang, L.; Yoon, M.-H.; Lu, G.; Yang, Y.; Facchetti, A.; Marks, T. J. *Nature Mater.* **2006**, *5*, 893−900.
(2) Huang, H.; Lee, Y. C.; Tan, O. K.; Zhou, W.; Peng, N.; Zhang, Q. *Nanotechnology* **2009**, *20*, 115501.
(3) Liu, Z.; Zhang, D.; Han, S.; Li, C.; Tang, T.; Jin, W.; Liu, X.; Lei, B.; Zhou, C. *Adv. Mater.* **2003**, *15*, 1754−1757.
(4) Ogale, S.; Choudhary, R.; Buban, J.; Lofland, S.; Shinde, S.; Kale, S.; Kulkarni, V.; Higgins, J.; Lanci, C.; Simpson, J.; Browning, N.; Das Sarma, S.; Drew, H.; Greene, R.; Venkatesan, T. *Phys. Rev. Lett.* **2003**, *91*, 1−4.
(5) Fitzgerald, C.; Venkatesan, M.; Dorneles, L.; Gunning, R.; Stamenov, P.; Coey, J.; Stampe, P.; Kennedy, R.; Moreira, E.; Sias, U. *Phys. Rev. B* **2006**, *74*, 1−10.
(6) Djurisić, A. B.; Leung, Y. H. *Small* **2006**, *2*, 944−61.
(7) Könenkamp, R.; Word, R. C.; Schlegel, C. *Appl. Phys. Lett.* **2004**, *85*, 6004.
(8) Dai, Z. R.; Gole, J. L.; Stout, J. D.; Wang, Z. L. *J. Phys. Chem. B* **2002**, *106*, 1274−1279.
(9) Morales, A. M.; Lieber, C. M. *Science* **1998**, *279*, 208−211.
(10) Martin, C. R. *Science* **1994**, *266*, 1961−1966.
(11) Lakshmi, B. B.; Dorhout, P. K.; Martin, C. R. *Chem. Mater.* **1997**, *9*, 857−862.

(12) Cao, G.; Liu, D. *Adv. Colloid Interface Sci.* **2008**, *136*, 45−64.
(13) Cheng, B.; Russell, J. M.; Shi, W.; Zhang, L.; Samulski, E. T. *J. Am. Chem. Soc.* **2004**, *126*, 5972−5973.
(14) Dai, Z. R.; Pan, Z. W.; Wang, Z. L. *Adv. Funct. Mater.* **2003**, *13*, 9−24.
(15) Hu, J. Q.; Bando, Y.; Liu, Q. L.; Golberg, D. *Adv. Funct. Mater.* **2003**, *13*, 493−496.
(16) Duan, X.; Lieber, C. M. *Adv. Mater.* **2000**, *12*, 298−302.
(17) Dolbec, R.; El Khakani, M. A. *Appl. Phys. Lett.* **2007**, *90*, 173114.
(18) Barsan, N.; Weimar, U. *J. Electroceram.* **2001**, *7*, 143−167.
(19) Gordon, R. G. *MRS Bull.* **2000**, 52−57.
(20) He, J. H.; Wu, T. H.; Hsin, C. .; Li, K. M.; Chen, L. J.; Chueh, Y. L.; Chou, L. J.; Wang, Z. L. *Small* **2006**, *2*, 116−20.
(21) Huang, H.; Tan, O. K.; Lee, Y. C.; Tse, M. S.; Guo, J.; White, T. *Nanotechnology* **2006**, *17*, 3668−3672.
(22) Gu, F.; Wang, S.; Cao, H.; Li, C. *Nanotechnology* **2008**, *19*, 095708.
(23) Qin, L.; Xu, J.; Dong, X.; Pan, Q.; Cheng, Z.; Xiang, Q.; Li, F. *Nanotechnology* **2008**, *19*, 185705.
(24) Paraguay-Delgado, F.; Antúnez-Flores, W.; Miki-Yoshida, M.; Aguilar-Elguezabal, A.; Santiago, P.; Diaz, R.; Ascencio, J. A. *Nanotechnology* **2005**, *16*, 688−694.
(25) Kawazoe, H.; Yasukawa, M.; Hyodo, H.; Kurita, M.; Yanagi, H.; Hosono, H. *Nature* **1997**, *389*, 939−942.
(26) Dijkkamp, D.; Venkatesan, T.; Wu, X. D.; Shaheen, S. a.; Jisrawi, N.; Min-Lee, Y. H.; McLean, W. L.; Croft, M. *Appl. Phys. Lett.* **1987**, *51*, 619−621.
(27) Narayan, J.; Dovidenko, K.; Sharma, A. K.; Oktyabrsky, S. *J. Appl. Phys.* **1998**, *84*, 2597−2601.
(28) Dominguez, J. E.; Fu, L.; Pan, X. Q. *Appl. Phys. Lett.* **2002**, *81*, 5168−5170.
(29) Jung, S. W.; An, S.-J.; Yi, G.-C.; Jung, C. U.; Lee, S.-I.; Cho, S. *Appl. Phys. Lett.* **2002**, *80*, 4561−3.
(30) Kim, H.; Piqué, A. *Appl. Phys. Lett.* **2004**, *84*, 218−20.
(31) Rijnders, G.; Blank, H. A. In *Pulsed Laser Ablation of Thin Films*; Eason, R., Ed.; John Wiley & Sons, Inc.: Hoboken, NJ, 2007; pp 177−190.
(32) Tien, L. C.; Pearton, S. J.; Norton, D. P.; Ren, F. *Appl. Phys. A: Mater. Sci. Process.* **2008**, *91*, 29−32.
(33) Bond, G. C.; Louis, C.; Thompson, D. T. *Catalysis by Gold*; Imperial College Press: London, 2006.
(34) Jalili, H.; Heinig, N. F.; Leung, K. T. *J. Chem. Phys.* **2010**, *132*, 204701.
(35) Kern, W. *Handbook of Semiconductor Wafer Cleaning Technology*; William Andrew Publishing/Noyes: Norwich, NY, 1993.
(36) Sohn, Y.; Pradhan, D.; Radi, A.; Leung, K. T. *Langmuir* **2009**, *25*, 9557−63.
(37) Batzill, M.; Diebold, U. *Prog. Surf. Sci.* **2005**, *79*, 47−154.